Joint tomographic inversion of first-arrival and reflection traveltimes for recovering 2-D seismic velocity structure with an irregular free surface

XinYan Zhang[1]*, ZhiMing Bai[2]*, Tao Xu[2,3], Rui Gao[4,1], QiuSheng Li[1], Jue Hou[5], and José Badal[6]

[1]Key Laboratory of Deep-Earth Dynamics of Ministry of Land and Resources, Institute of Geology, Chinese Academy of Geological Sciences, Beijing 100037, China;

[2]State Key Laboratory of Lithospheric Evolution, Institute of Geology and Geophysics, Chinese Academy of Sciences, Beijing 100029, China;

[3]CAS Center for Excellence in Tibetan Plateau Earth Sciences, Beijing 100101, China;

[4]School of Earth Science and Engineering, Sun Yat-sen University, Guangzhou 510275, China;

[5]Institute of Geophysics, China Earthquake Administration, Beijing 100081, China;

[6]Physics of the Earth, Sciences B, University of Zaragoza, Spain

Abstract: Irregular surface flattening, which is based on a boundary conforming grid and the transformation between curvilinear and Cartesian coordinate systems, is a mathematical method that can elegantly handle irregular surfaces, but has been limited to obtaining first arrivals only. By combining a multistage scheme with the fast-sweeping method (FSM, the method to obtain first-arrival traveltime in curvilinear coordinates), the reflected waves from a crustal interface can be traced in a topographic model, in which the reflected wavefront is obtained by reinitializing traveltimes in the interface for upwind branches. A local triangulation is applied to make a connection between velocity and interface nodes. Then a joint inversion of first-arrival and reflection traveltimes for imaging seismic velocity structures in complex terrains is presented. Numerical examples all perform well with different seismic velocity models. The increasing topographic complexity and even use of a high curvature reflector in these models demonstrate the reliability, accuracy and robustness of the new working scheme; checkerboard testing illustrates the method's high resolution. Noise tolerance testing indicates the method's ability to yield practical traveltime tomography. Further development of the multistage scheme will allow other later arrivals to be traced and used in the traveltime inversion.

Keywords: irregular surface flattening; boundary conforming grid; multistage scheme; traveltime tomography

1. Introduction

The orogenic belts as well as basin-mountain coupling regions always have strongly varying topographies, which makes rather difficult the accurate reconstruction of subsurface structures. This problem is quite common because seismic observations are usually made on such irregular structures as orogenic belts, basins, and transition zones (Teng JW et al., 1987, 2003; Kaila and Krishna, 1992; Zeng RS et al., 1995; Li SL and Mooney, 1998; Artemieva, 2003; Carbonell et al., 2004; Gao R et al., 2005; Wu CL et al., 2005; Wang CY et al., 2000, 2007; Bai ZM et al., 2007; Zhang ZJ and Klemperer, 2005, 2010; Tian XB et al., 2011; Zhang ZJ et al., 2011). In this context, achieving accurate traveltime tomography for topo-

graphies that are irregular is essential to constructing high-accuracy models, whether based on conventional ray tracing (Julian and Gubbins, 1977; Cassell, 1982; Um and Thurber, 1987; Sambridge, 1990; Zelt and Smith, 1992; Koketsu and Sekine, 1998; Xu T et al., 2006, 2010, 2014) or on grid-based traveltime schemes (Vidale, 1988; Podvin and Lecomte, 1991; van Trier and Symes, 1991; Qin FH et al., 1992; Cao SH and Greenhalgh, 1994; Kim and Cook, 1999; Afnimar and Koketsu, 2000; Qian JL and Symes, 2002). The grid-based solvers have proven to be considerably faster than classical ray tracing, and problems such as shadow zones, multipathing, and barrier penetration can be easily handled.

Most modern tomographic techniques addressing an irregular surface are based on unstructured grids, which is computationally inefficient in model parameterization and traveltime calculation (Kimmel and Sethian, 1998; Sethian, 1999; Sethian and Vladimirsky, 2000; Rawlinson and Sambridge, 2004a, b; Qian JL et al. 2007a, b; Kao CY et al., 2008; Lelièvre et al., 2011). Unlike these techniques, the structured grid-based schemes usually handle ir-

regular surfaces by using model expansion (Vidale, 1988; Reshef, 1991; Hole, 1992; Ma T and Zhang Z, 2014a, b, 2015) or irregular surface flattening (Haines, 1988; Lan HQ and Zhang ZJ, 2011a, b, 2013a, b; Lan HQ et al., 2012). The former scheme usually employs a stair-step approximation of the irregular surface or a flat low-velocity layer covering the surface, which may cause accuracy loss and even distorted images. The latter scheme takes advantage of a boundary conforming grid and a transformation from Cartesian to curvilinear coordinates, allowing the irregular topographic model to be mathematically flattened. In this method, first-arrival traveltimes can be obtained by solving the topography-dependent eikonal equation (hereafter TDEE) (Lan HQ and Zhang ZJ, 2013a).

On the other hand, reflected waves revealed by deep seismic reflection profiling may be numerous and even have large amplitude if the seismic impedance is great; they can be very useful in probing the crust, and are therefore potentially a valuable resource for seismic imaging. Reflected waves also contain information of both the velocity of the elastic medium and the seismic reflector and hence can be used to make joint inversion for velocity structure and interface depths (Li SL and Mooney, 1998; Knapp et al., 2004; Scarascia and Cassinis, 1997; Zhang ZJ and Klemperer, 2010), which is a natural complement of migration imaging (Rawlinson and Goleby, 2012). Having a larger set of seismic first-arrival and reflection data and the right tool to carry out joint inversion of all of them is a task worth addressing. A number of grid-based schemes have been proposed for tracking reflected waves, such as the two-way approach and the multistage scheme, but most of them are based on the assumption of a flat surface and therefore cannot be used with irregular topography (Benamou, 1996; Symes and Qian JL, 2003; Podvin and Lecomte, 1991; Riahi and Juhlin, 1994).

The aim of this paper is to obtain accurate seismic velocity models for irregular free surfaces, by using a mathematical surface flattening strategy and a multistage working scheme and by taking advantage of first-arrival and reflection traveltime data provided by deep seismic experiments. To obtain first-arrival traveltimes we use the fast-sweeping method (FSM) to solve TDEE formulated in curvilinear coordinates. To track reflected waves on a crustal interface we use a multistage scheme via first-arrival wavefront solved by FSM. We then present a joint inversion method of first-arrival and reflection traveltimes to determine velocity models for an irregular surface. We have arranged this paper as follows: first, we briefly describe the irregular surface flattening scheme, including

the boundary conforming grid, the topography-dependent eikonal equation, and the method for computation of first-arrival traveltimes and ray paths. Next, we introduce the method for computation of reflection traveltimes and ray paths, and then the joint inversion of first-arrival and reflection traveltimes (JI-FRRT), including the inversion strategy. Finally, we present several numerical examples to illustrate the performance of JI-FRRT, which demonstrate the potential applications of this methodology to reveal the internal structure of the earth through modeling seismic velocity.

2. Theory

2.1 Topography-Flattening Scheme and Topography-Dependent Eikonal Equation in 2-D

The topography-flattening is achieved by transforming the Cartesian coordinate system to a curvilinear coordinate system, using grids conforming to the irregular surface to describe the model (Figure 1). Such a grid is called a "boundary-conforming grid" (Thompson et al., 1985; Hvid, 1994), and has been used by many researchers (Fornberg, 1988; Zhang W and Chen XF, 2006; Appelo and Petersson, 2009; Lan HQ and Zhang ZJ, 2011a, b, 2013a, b). Under such a transformation, the curvilinear coordinates (q, r) in the mathematical space are mapped onto the Cartesian coordinates (x, z) in the physical space. Hence, a topographic physical model (x, z) is converted to a flattened mathematical model (q, r) (in the mathematical space) (Figure 1). Neighboring elements in the physical space are also adjacent in the mathematical space. Velocity nodes of the models are given at the curvilinear coordinates, but transformed and expressed in the physical space (x, z). Note that the irregular surface should be second-order derivable to insure an efficient computation.

Using the topography-flattening method, the classical eikonal equation expressed in Cartesian coordinates becomes a new generalized equation in the curvilinear coordinate system, which is topography-dependent (Lan HQ and Zhang ZJ, 2013a, b):

$$A \cdot \left(\frac{\partial T(x,z)}{\partial q} \right)^2 + B \cdot \frac{\partial T(x,z)}{\partial q} \frac{\partial T(x,z)}{\partial r} + C \cdot \left(\frac{\partial T(x,z)}{\partial r} \right)^2 = s^2(q,r) \tag{1}$$

with $A = \frac{1}{J^2}(x_r^2 + z_r^2), B = -\frac{2}{J^2}(x_q x_r + z_q z_r), C = \frac{1}{J^2}(x_q^2 + z_q^2)$.

The "coefficients" A, B and C are topography-dependent. T is traveltime, s is slowness, J is the Jacobian that is written as $J = x_q z_r - x_r z_q$ and x_q denotes $\partial q(x,z)/\partial x$, and similar in other cases.
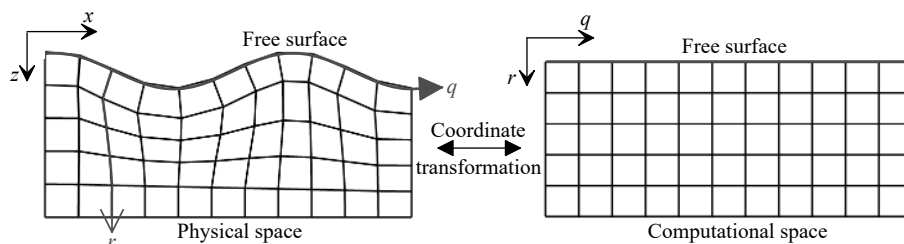

Figure 1.   Irregular surface flattening scheme: transformation between Cartesian coordinates (x, z) and curvilinear coordinates (q, r) based on a boundary conforming grid.

Zhang X Y et al.: Joint tomography for structure with irregular surface

The Lax-Friedrichs sweeping scheme, a fast-sweeping method (hereafter FSM), is applied to solve equation (1) and to obtain the first-arrival times. We determine the ray paths following the steepest traveltime gradient in the curvilinear system from the receiver to the source (Ma T and Zhang ZJ, 2014). Traveltimes at receivers and shots are calculated by interpolation to trace their positions exactly.

2.2 Multistage Scheme for Reflection Tracking

Traditional grid-based eikonal schemes for computing traveltimes are usually limited to obtaining first arrivals only (Rawlinson et al., 2004a), not excluding the topography-dependent eikonal equation. A multistage scheme is an efficient method for tracking later arrivals in layered media, and has been successfully used by some researchers in combination, respectively, with the fast-marching method (Rawlinson and Sambridge, 2014a, b) or the shortest-path method (Bai et al., 2009, 2010; Huang GJ et al., 2012). The former has not considered an irregular surface; the latter can handle the irregular problem but is time-consuming. In this paper, we try to combine the multistage scheme with a topography-dependent eikonal equation to trace reflected phase exactly in an irregular model. The two principal difficulties involved in introducing a multistage scheme is (1) how to combine it with first-arrivals' numerical solution processing (FSM); (2) how to represent accurately the reflecting interface, which generally varies with depth and does not conform to the regular velocity grid.

Faithful representation of the reflection interface was solved by introducing a set of nodes that irregularly lie on the interface and are independent from the velocity grid nodes. A connectivity between the irregular interface nodes and the regular grid nodes was constructed by local triangulation in the neighborhood of the interface; traveltimes at the interface nodes were attained by a linear interpolation scheme of the triangle with two points in the velocity grid (Figure 2b).

We adopted the multistage method, in combination with the FSM, for the numerical solution of the TDEE (called multistage FSM), to calculate reflected phases in layered media with an irregular surface. The multistage FSM scheme involves four stages (Figure 2): the first stage initializes FSM at the source and tracks the incident wave front to all points on the reflecting interface (Figure 2a); the second stage records traveltimes of first arrivals along the sampled interface, applying the local triangle linear-interpolation to calculate traveltimes on interface nodes from those on velocity nodes (Figure 2b); the third stage tracks the reflected wave front by reinitializing FSM from the sampled interface (Figure 2c); the fourth stage tracks ray paths along the negative gradient direction of the obtained traveltime field, from receivers to the reflector and then to sources (Figure 2d).

Since the multistage FSM is established by initializing the wave front from interfaces, later arrivals that propagate in multiple layered media can be correctly computed by following the propagating step. In this paper, we solve the topography case with an irregular surface on the top simply by extending the multistage FSM to 2-D curvilinear coordinates with a single reflector.

3. Tomographic Inversion

3.1 Back-Projection Algorithm

The inversion is carried out by a back-projection algorithm (Hole, 1992), in which the traveltime residues are uniformly projected along ray paths. Thereafter, the slowness perturbation δs in each grid cell can be written as:

$$\delta s = \frac{1}{K} \sum \frac{\delta t_k}{l_k}, k = 1, 2, ..., K, \qquad (2)$$

here K is the number of rays passing through any of the neighboring cells, δt_k and l_k are respectively the traveltime residue and the
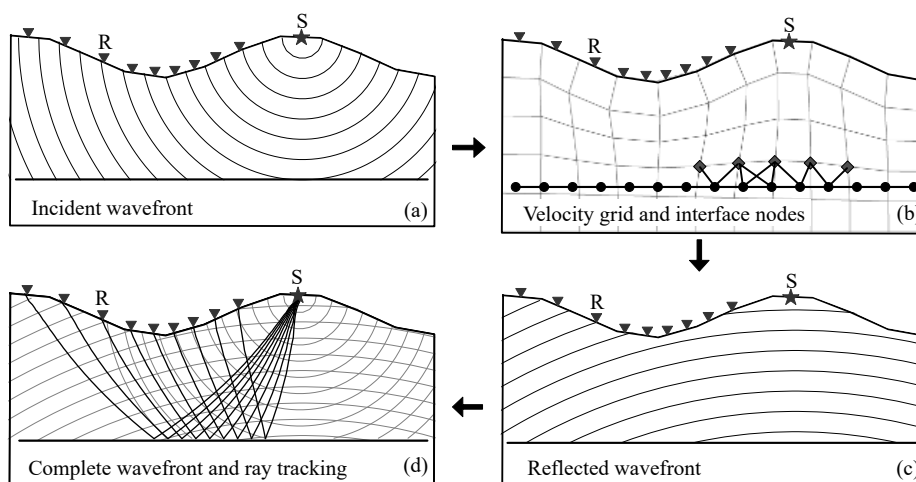

Figure 2. (a) Incident wavefront is tracked from source to all points on the reflecting interface; (b) Interface nodes (black circles) are independent from the velocity grid nodes (gray diamonds), and traveltimes at interface nodes are obtained from those at velocity nodes by a local triangle linear-interpolation; (c) Reflected wavefront is tracked to receivers on the surface; (d) Ray paths are tracked along the negative gradient direction of the obtained traveltime field, from receivers to the reflector and then to sources. Source (S) and receivers (R) are denoted by star and triangles, respectively.

total length of the *k*-th ray. The slowness perturbation is calculated in the ray tracing process, which belongs to the forward process. As the model is parameterized at grid points, the slowness perturbation at each grid point is found by taking the average of the values obtained from the cells surrounding this grid point. The inversion grid is a larger grid resampled from the grid used in the forward calculation; a smoothing factor is introduced to spread the slowness perturbation over a wider area and decrease local velocity anomalies. An appropriate choice of the resample and the smoothing factor ensures that the velocity model will be well updated. The velocity model is updated by iteration until the traveltime residue is sufficiently small and does not change significantly with the next iteration.

3.2 Joint Inversion Strategy

The use of first-arrival waves together with reflected waves identified from a deep seismic sounding experiment requires joint inversion strategies. For the sake of simplicity, in this article we assume a specified reflector to take care of exploring the seismic velocity structure of the medium; in other words, in the inversion process we set the reflection interface and try to obtain an accurate velocity image.

In the inversion process, a back-projection algorithm is applied, respectively, to the first-arrival and the reflection phases, and the slowness perturbations are calculated along each phases' paths, respectively. We then sum up the two classes of perturbations in each cell, to update the velocity (slowness) model. The use of the total slowness perturbation to update the velocity model at each iterative step allows us to obtain the final velocity model. Figure 3

shows a flow-chart that describes the JI-FRRT process.

In order to avoid large perturbations and over fitting of noise when applying the inversion routine in the computational domain, we first take the smoothing factor in the horizontal direction equaling to n_x (the number of nodes in the horizontal direction), to keep the velocity fixed in this direction and only updated in the vertical direction. After an applicable 1-D model is obtained, we adjust the smoothing operator in both directions to update the velocity and finally obtain a 2-D model.

4. Numerical Examples

Below we develop several numerical examples in order to verify the performance of JI-FRRT. First, we consider three models having increasing topographic complexity, and an undulated reflector to prove the accuracy of the traveltime joint inversion procedure. Second, we analyze the quality of the results through the classical checkerboard test. Third, we also check the efficiency of the method assuming a model with irregular topography and an undulated reflector, together with an intracrustal high-velocity body. Lastly, we test the robustness of our working scheme by checking its noise tolerance. In all tests, the first-arrival and reflection traveltimes at each receiver, i.e., the input data for further seismic modeling, are calculated by forward process of JI-FRRT, by using theoretical models those to be inverted.

4.1 Different Topographic Complexities

We consider three topographic models labeled as Models 1, 2 and 3. Model 1 has a trapezoidal hill located in the middle of the mod-
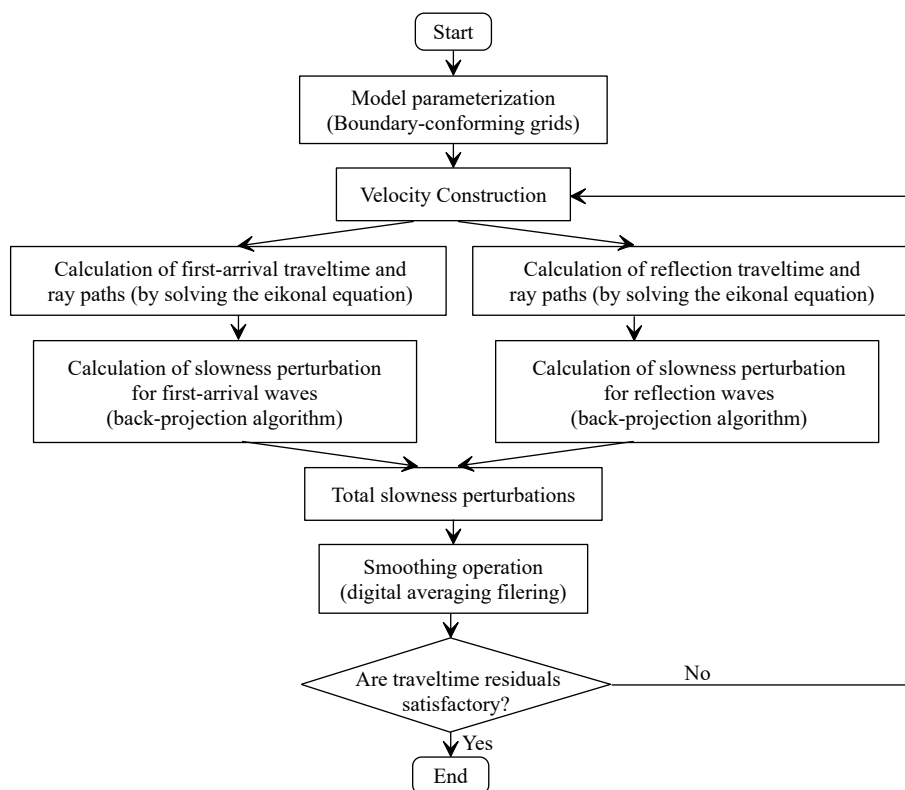

Figure 3. Flow-chart describing the joint tomographic inversion of first-arrival and reflection traveltimes.

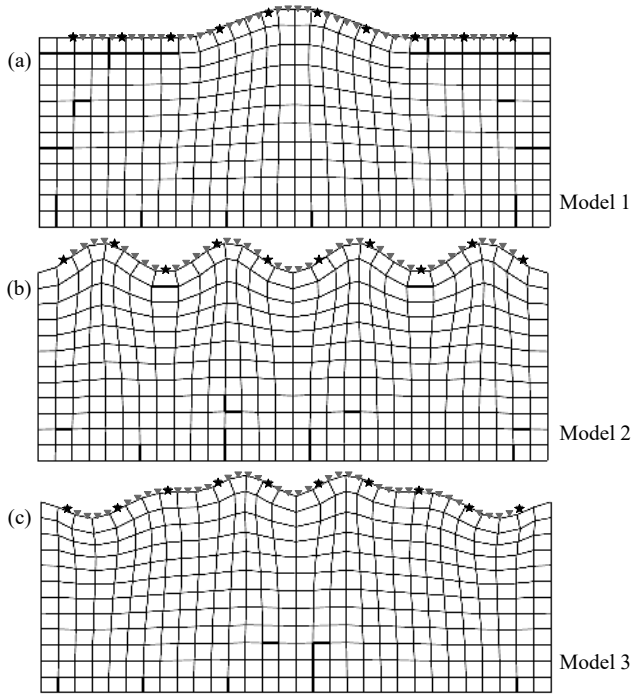**Zhang X Y et al.: Joint tomography for structure with irregular surface**

Figure 4. Three structural models each with irregular free surface of different complexity: (a) a single centered trapezoidal hill (Model 1); (b) 4 hills and 3 valleys uniformly conforming the ground surface (Model 2); (c) two hills combined with two valleys (Model 3). In all cases the boundary conforming grid is integrated by a mesh with 100 × 50 cells that is displayed with a density reduction factor of 3. Stars indicate up to ten shots, and the inverted triangles the location of 46 receivers evenly spaced on the irregular surface.

el surface (Figure 4a). Model 2 consists of 4 hills and 3 valleys uniformly arranged on its surface (Figure 4b). Model 3 is the one that has the most complex topographic surface, since it combines hills and valleys irregularly (Figure 4c). The topographic gradients were

designed to increase gradually from Model 1 to Model 3 with the aim of testing the reliability and accuracy of JRFTT under different topographic complexities. We made several tomographic inversions using different grids, and found that the optimal grid spacing was 0.5 km in both vertical and horizontal directions. Figure 4 shows the model mesh 100 × 51 (number of grid nodes in the horizontal and vertical directions) displayed with a density reduction factor of 3, which represents the boundary-conforming grid for the three models, with a grid spacing of about 1.5 km. As before, we fired 10 shots that were recorded by 46 receivers evenly arranged on the irregular topographic surface. In order to include a non-flat reflective surface, thereby increasing the complexity of the initial model and bringing us closer to a real case, we introduced an undulated interface in the velocity field lying at the depth range 21–33 km. Then we carried out several inversions with different re-gridding and moving average factors, and finally found the optimal factors to be, respectively, (4, 2) and (5, 3) for all three tests.

We pick 460 first-arrival and 460 reflection traveltimes to image the model, which is parameterized by grids of size (101 × 51). Figures. 5a, b, and c show the tomography results for Models 1, 2, and 3, respectively. In all plots the continuous line denotes the wavy reflection interface. We can see the theoretical velocity models (upper panels), the initial models (middle panels), and the inverted models (lower panels) obtained by JI-FRRT. The results reconstruct the theoretical models with very little error, even with increasing topography complexities and starting from an initial model that clearly deviates from the target model.

After obtaining the inversion solutions, we are interested in estimating the quality (accuracy) of the results. Thus we evaluate the results based on the following criteria. First, since our working scheme updates the velocity along the ray paths, we need to display the ray geometry and the ray coverage density, i.e. the number of rays that cross each grid cell. This information is given in Figure 6, which reveals the illumination of the explored medium.
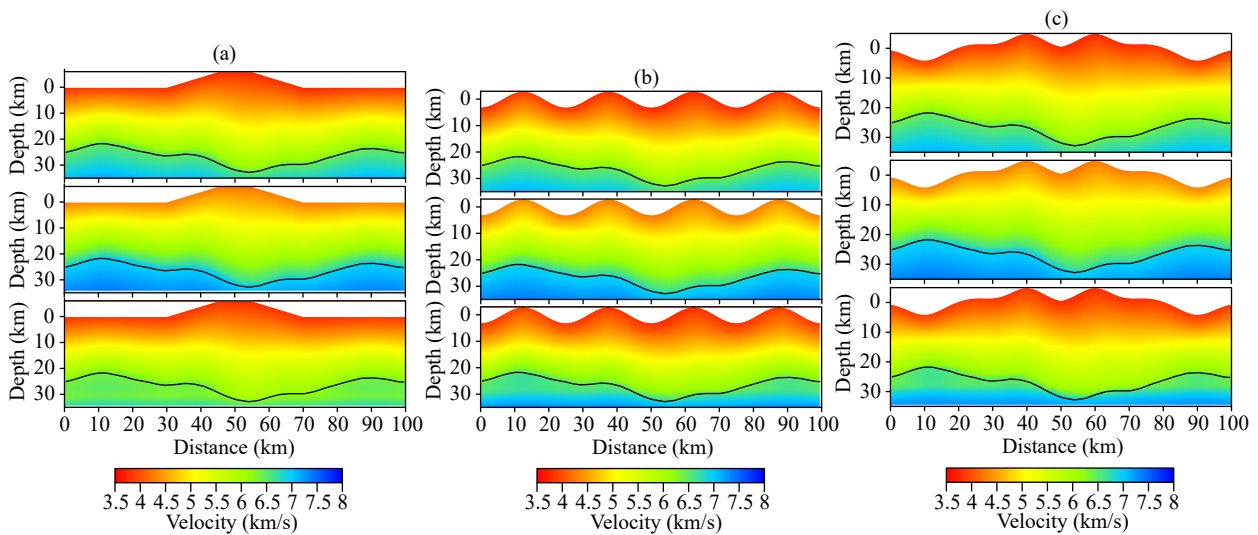

Figure 5. P-wave velocity models with the topography of Model 1 (a), Model 2 (b) and Model 3 (c). The top panels are theoretical models, the middle panels are initial models, and the lower panels are inverted models; the continuous line in each figures denotes the same wavy reflection interface.
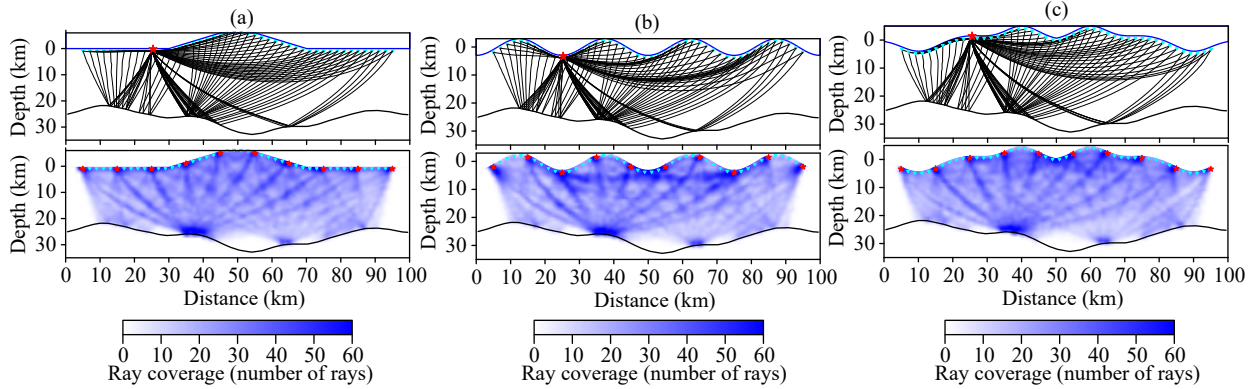
Figure 6. Ray coverage with reference to the model shown in Figure 5, respectively for Model 1 (a), Model 2 (b) and Model 3 (c). The upper panels are raypaths from the 3rd shot, and the lower panels are number of rays that intersect each cell. Sources (stars) and receivers (triangles) are evenly spaced on the irregular surface.
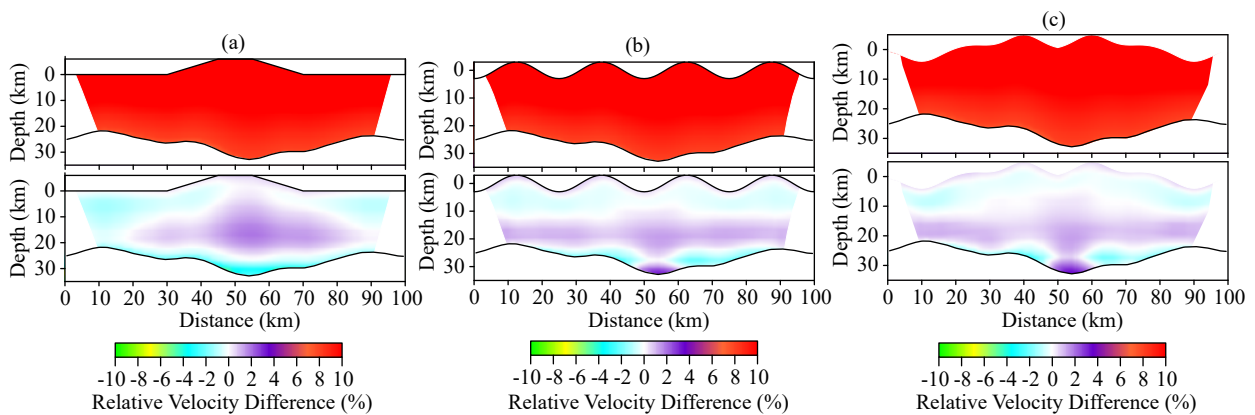

Figure 7. Relative velocity errors of initial models (the upper panels) and inverted models (the lower panels), all compared to theoretical models shown in the upper panels of Figure 5. Just the regions with denser ray coverage (>5 rays passing through each cell) are shown.

Second, it is necessary to estimate the error made in the calculation of the solution. With respect to the regions with denser ray coverage (>5 rays passing through each cell), Figure 7 shows the relative velocity error regarding the final inverted models (lower panels) and that inherent to the initial models (upper panels), both compared to the theoretical models. As can be seen, the former are much smaller than the latter ones, the initial error being larger than 10% and the final error smaller than 3%, especially for the middle region above the reflection interface. Third, RMS traveltime residues versus number of iterations demonstrate the rapid convergence of the inversion for each of the three numerical examples (Figure 8). After about five iterations, the residues gradually stabilize and converge to approximately 0.004 s in all cases. Both the convergence of traveltime residues and the convergence of velocity errors to very small values demonstrate the consistency of JI-FRRT.

In order to evaluate the vertical and horizontal resolution of our inversion scheme, we also perform the checkerboard test for Models 1, 2, and 3. The models are divided artificially into zones of relatively high and low velocity at a scale of 7.5 km × 7.5 km, so that velocity anomalies described by the formula 0.3 × sin(x) × sin(z) are added alternatively to a common reference velocity for all models (upper panels in Figure 9). The synthetic traveltime is
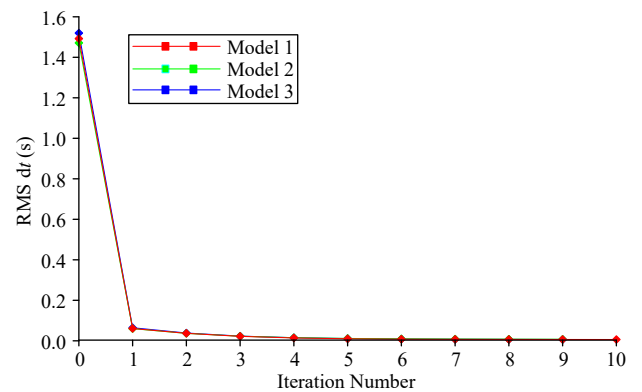

Figure 8. RMS traveltime residues vs. number of iterations in relation to the three prior models (Figures 5a, b, and c).

obtained from the checkerboard model; the common reference velocity is taken from the initial model. In the inversion process, the rays are unevenly distributed in the model due to the undulated reflector, so the recovered velocity field is closely related to the weighted ray density. Upper panels in Figure 9 show theoretical checkerboards, while lower panels in Figure 9 are reconstructed checkerboards, which reproduce the target velocity values
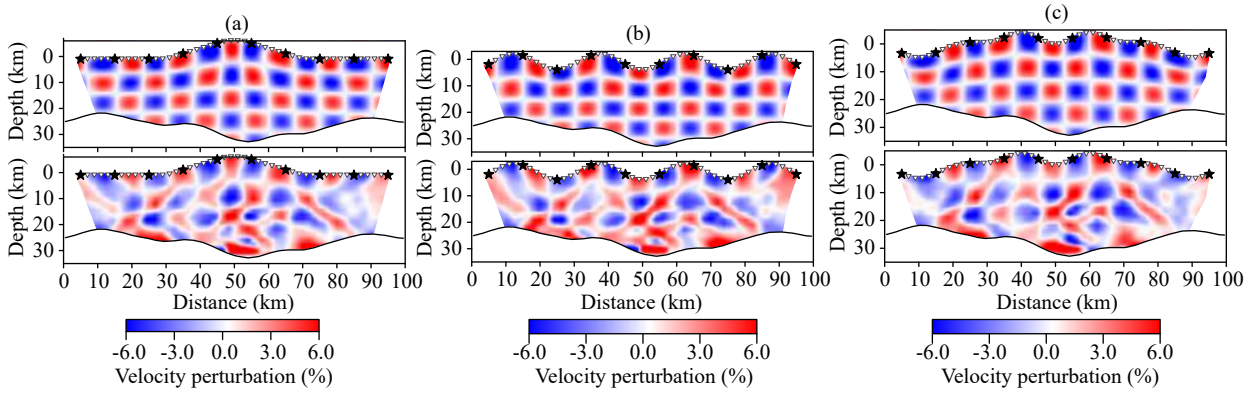
Figure 9.   Checkerboard tests for models 1, 2, and 3 (Figures 5a, b, and c). The upper panels show original checkerboard models, while the lower panels are the corresponding reconstructed checkerboards. Sources (stars) and receivers (triangles) are positioned identically on the irregular surface.
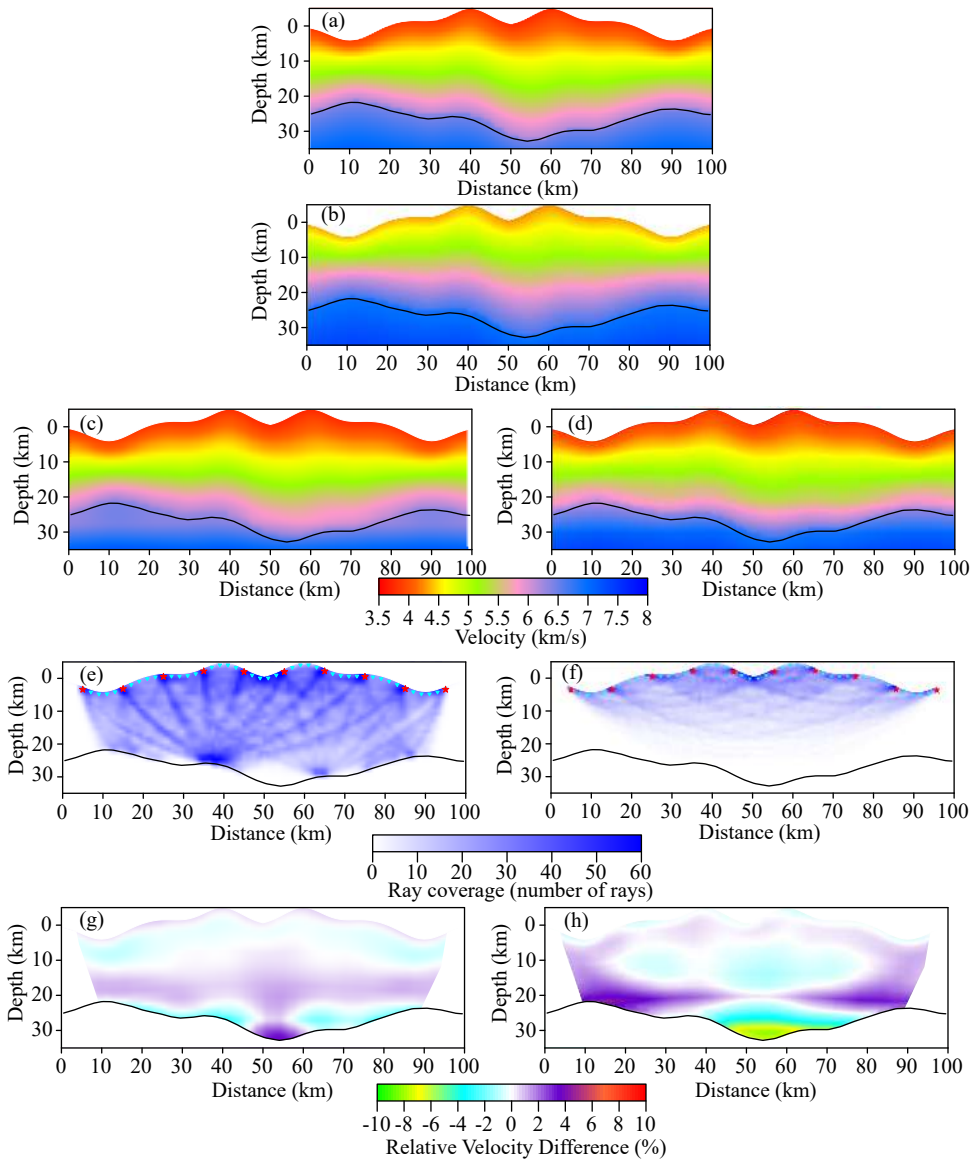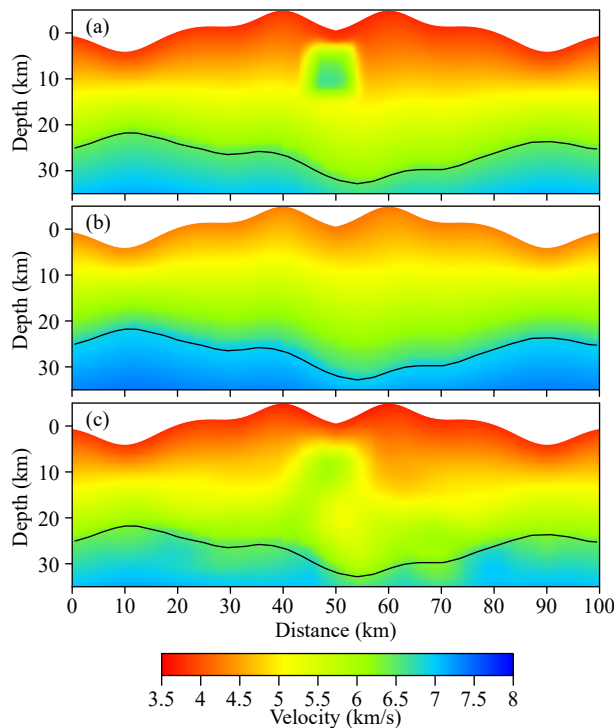

Figure 10.   The contrasting results and other relevant outputs of JI-FRTT and first-arrival tomography. From top to bottom: (a) P-wave velocity distribution depicting the theoretical model, (b) initial model, (c) tomographic image obtained by JI-FRRT, (d) tomographic image obtained by the first-arrival tomography, (e) number of rays that intersect each grid cell for JI-FRRT, (f) number of rays that intersect each grid cell for first-arrival tomography, (g) inverted velocity anomaly for JI-FRRT, (h) inverted velocity anomaly for first-arrival tomography.

Zhang X Y et al.: Joint tomography for structure with irregular surface

quite well, particularly in zones where there are a larger number of rays crossing the medium. This illustrates that our scheme indeed has high resolution in the vertical and horizontal directions.

4.2 Comparing with First-Arrival Tomography

As the reflection phase is used to probe a deeper area, compared with the first-arrival tomography (Ma T and Zhang ZJ, 2015), we conduct a first-arrival tomography to make a comparison with the muti-phase tomography. The contrasting results and other relevant outputs are shown in Figures 10a–h. From top to bottom: (a) P-wave velocity distribution depicting the theoretical model, (b) initial model, (c) tomographic image obtained by JI-FRRT, (d) tomographic image obtained by the first-arrival tomography, (e) number of rays that intersect each grid cell for JI-FRRT, (f) number of rays that intersect each grid cell for first-arrival tomography, (g) inverted velocity anomaly for JI-FRRT, (h) inverted velocity anomaly for first-arrival tomography. Since the first-arrival rays can travel only in a shallow area (Figures 10e–f), the velocity difference of the first arrival result is larger than that of JI-FRRT, especially at the deeper area near the reflector (Figures 10g–h).

4.3 High-Velocity Anomaly

To check the efficiency of the method we now take a model based on previous Model 3 that irregularly combines hills and valleys (Figure 4c) and has an intracrustal high-velocity body. We add a high-velocity anomaly (+ 2 km/s) with size 14 km × 14 km just below the central valley of the test structure (Figure 4c). The inversion result and other relevant outputs are shown in Figures 11a–g. From top to bottom: (a) P-wave velocity distribution depicting the theoretical model, (b) initial model, (c) tomographic image obtained by JI-FRRT, (d) ray diagram from the 3rd shot point, (e) number of rays that intersect each grid cell, (f) theoretical velocity anomaly, (g) inverted velocity anomaly. A slight focusing of the rays takes place in the anomaly zone (Figure 11e). All these results illustrate that the velocity anomaly can be reconstructed with success using JI-FRRT.

4.4 Noise Tolerance

The inversion algorithm is known to work well with noise-free data, but this might not be the case with noise-contaminated data
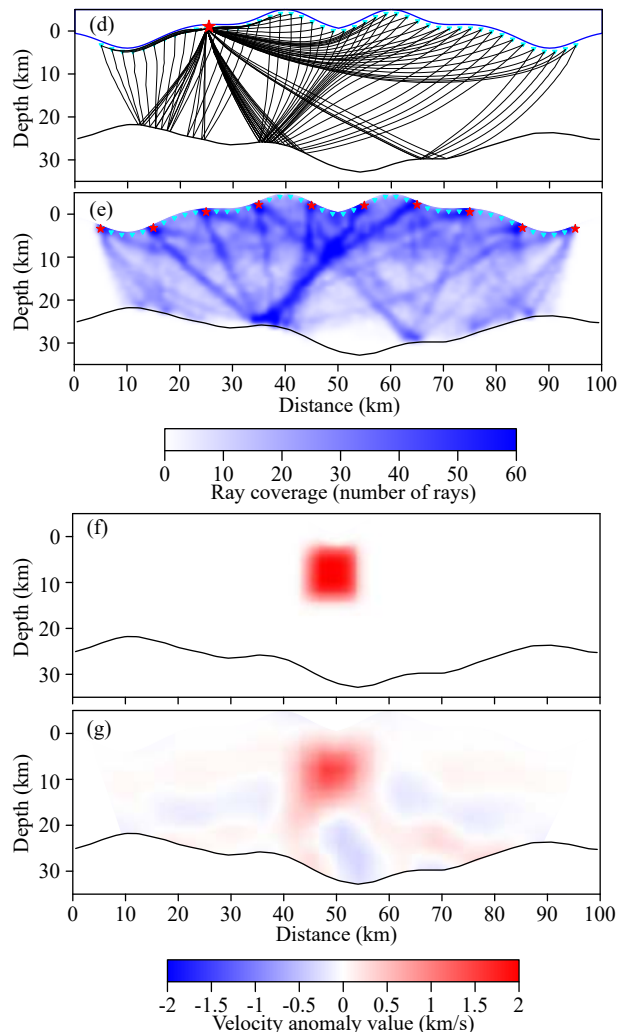

Figure 11. Test with a high-velocity body embedded within the model shown in Figure 5c. From top to bottom: (a) P-wave velocity distribution depicting the theoretical model, (b) initial model, (c) tomographic image obtained by JI-FRRT, (d) ray diagram from the 3rd shot point, (e) number of rays that intersect each grid cell, (f) theoretical velocity anomaly, (g) inverted velocity anomaly.

(Zhou B et al., 1992). To determine the response of JI-FRRT to data contaminated by noise, we added random Gaussian noise with standard deviation of $\sigma = 0.2$ s to the synthetic data computed from Model 3 (Figure 4c). The inversion result and other relevant outputs are shown in Figures 12a–g. From top to bottom: (a) theoretical model, (b) initial model, (c) tomographic model obtained by JI-FRRT, (d) ray diagram, (e) ray coverage, (f) relative velocity error inherent to the initial model, (g) relative velocity error regarding the final inverted model. Although the velocity error is a little larger than in the noise-free case (lower panel in Figure 7c), the new tomographic image (Figure 12c) fits well to that of the theoretical model (Figure 12a) and is comparable to the image obtained before without noise (lower panel in Figure 5c). This further supports the robustness of JI-FRRT by demonstrating that our inversion scheme works well even with noisy data.

5. Conclusion

We present a tomographic inversion method to determine the seismic velocity structure of a physical domain whose topograph-ic surface is irregular or non-flat. To deal with this physical feature, we employ the mathematical tool called irregular surface flattening, which is based on the use of a boundary conforming grid and the transformation between curvilinear and Cartesian coordinates. The method has been designed to jointly invert first-arrival and reflection traveltimes (JI-FRRT). The fast-sweeping method (FSM) is applied to a topography-dependent eikonal equation (TDEE) in curvilinear coordinates to obtain first-arrival traveltimes; the multistage scheme is introduced to combine with FSM to propagate reflected waves from an interface. The reflection paths are traced along the negative gradient direction of the traveltime field from receiver to source. We calculate slowness perturbations using first-arrival and reflection paths and the back-projection algorithm, and then we sum these results to update the velocity model.

Numerical examples reveal that JI-FRRT performs well. Tests performed with models of increasing topographic complexity and an undulated reflection interface support the reliability and accuracy
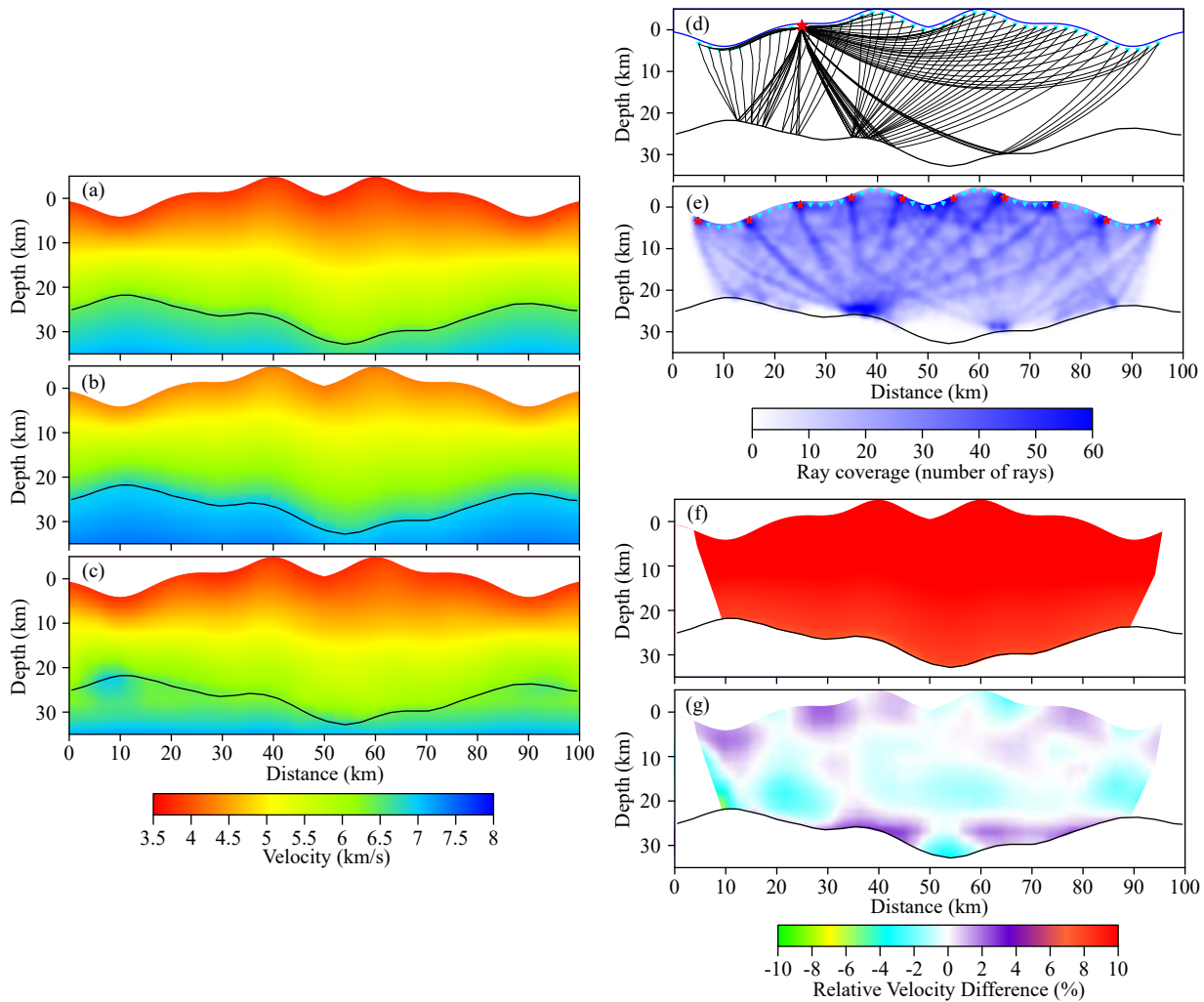

Figure 12. Noise tolerance of the inversion scheme. Random Gaussian noise with standard deviation of $\sigma = 0.2$ s was added to the synthetic traveltime data for both first arrivals and reflected waves, for computation with the model shown in Figure 8c. From top to bottom: (a) theoretical model, (b) initial model, (c) tomographic model obtained by JI-FRRT, (d) ray diagram from the 3rd shot point, (e) ray coverage, (f) relative velocity error inherent to the initial model, (g) relative velocity error regarding the final inverted model.

of JI-FRRT on the basis of the final tomographic model, ray diagram and ray density coverage, small error in the solution, and rapid convergence of the computational algorithm. Moreover, the classical checkerboard test also indicates that the spatial resolution of JI-FRRT is quite acceptable. The efficiency of JI-FRRT in detecting a velocity anomaly in the interior of the crust is another attractive feature of the method. Finally, JI-FRRT shows a good noise tolerance, which is an important issue when one is working with field data.

In the near future we hope to apply the inversion scheme to other later arrival phases and to include the interface inversion in the scheme, to better apply it to more real travel-time processing.

Acknowledgements

References

Afnimar, and Koketsu, K. (2000). Finite difference traveltime calculation for head waves travelling along an irregular interface. *Geophys. J. Int.*, *143*(3), 729–734. https://doi.org/10.1046/j.1365-246X.2000.00269.x

Appelö, D., and Petersson, N. A. (2009). A stable finite difference method for the elastic wave equation on complex geometries with free surfaces. *Commun. Comput. Phys.*, *5*(1), 84–107.

Artemieva, I. M. (2003). Lithospheric structure, composition, and thermal regime of the East European Craton: implications for the subsidence of the Russian platform. *Earth Planet. Sci. Lett.*, *213*(3-4), 431–446. https://doi.org/10.1016/S0012-821X(03)00327-3

Bai, C. Y., Huang, G. J., and Zhao, R. (2009). 2-D/3-D irregular shortest-path ray tracing for multiple arrivals and its applications. *Geophys. J. Int.*, *183*(3), 1596–1612.

Bai, C. Y., Tang, X. P., and Zhao, R. (2009). 2-D/3-D multiply transmitted, converted and reflected arrivals in complex layered media with the modified shortest path method. *Geophys. J. Int.*, *179*(1), 201–214.

Bai, Z. M., Zhang, Z. J., and Wang, Y. H. (2007). Crustal Structure across the Dabie-Sulu orogenic belt revealed by seismic velocity profiles. *J. Geophys. Eng.*, *4*(4), 436–442. https://doi.org/10.1088/1742-2132/4/4/009

Benamou, J. D. (1996). Big ray tracing: Multivalued travel time field computation using viscosity solutions of the Eikonal equation. *J. Comput. Phys.*, *128*(2), 463–474. https://doi.org/10.1006/jcph.1996.0224

Cao, S. H., and Greenhalgh, S. (1994). Finite-difference solution of the eikonal equation using an efficient, first-arrival, wavefront tracking scheme. *Geophysics*, *59*(4), 632–643.

Carbonell, R., Simancas, F., Juhlin, C., Pous, J., Pérez-Estaún, A., Gonzalez-Lodeiro, F., Muñoz, G., Heise, W., and Ayarza, P. (2004). Geophysical evidence of a mantle derived intrusion in SW Iberia. *Geophys. Res. Lett.*, *31*(11), L11601. https://doi.org/10.1029/2004GL019684

Cassell, B. R. (1982). A method for calculating synthetic seismograms in laterally varying media. *Geophys. J. R. Astron. Soc.*, *69*(2), 339–354. https://doi.org/10.1111/j.1365-246X.1982.tb04953.x

Fornberg, B. (1988). The pseudospectral method: Accurate representation of interfaces in elastic wave calculations. *Geophysics*, *53*(5), 625–637.

Gao, R., Lu, Z. W., Li, Q. S., Guan, Y., Zhang, J. S., He, R. Z., and Hang, L. Y. (2005). Geophysical survey and geodynamic study of crust and upper mantle in the Qinghai-Tibet Plateau. *Episodes*, *28*(4), 263–273.

Haines, A. J. (1988). Multi-source, multi-receiver synthetic seismograms for laterally heterogeneous media using F-K domain propagators. *Geophys. J. Int.*, *95*(2), 237–260. https://doi.org/10.1111/j.1365-246X.1988.tb00465.x

Hole, J. (1992). Nonlinear high‐resolution three‐dimensional seismic travel time tomography. *J. Geophys. Res.*, *97*(B5), 6553–6562. https://doi.org/10.1029/92JB00235

Huang G. J., Bai C. Y., Zhu D. I., and Greenhalgh S. (2012). 2D/3D seismic simultaneous inversion for the velocity and interface geometry using multiple classes of arrivals. *Bull. Seismol. Soc. Am.*, *102*(2), 790–801. https://doi.org/10.1785/0120110155

Hvid, S. (1994). *Three Dimensional Algebraic Grid Generation*. Copenhagen, Denmark: Technical University of Denmark.

Julian, B. R., and Gubbins, D. (1977). Three-dimensional seismic ray tracing. *J. Geophys. Res.*, *43*, 95–113.

Kaila, K. L., and Krishna, V. G. (1992). Deep seismic sounding studies in India and major discoveries. *Curr. Sci.*, *62*(1-2), 117–154.

Kao, C. Y., Osher, S., and Qian, J. L. (2008). Legendre-transform-based fast sweeping methods for static Hamilton–Jacobi equations on triangulated meshes. *J. Comput. Phys.*, *227*(24), 10209–10225. https://doi.org/10.1016/j.jcp.2008.08.016

Kim, S., and Cook, R. (1999). 3-D traveltime computation using second-order ENO scheme. *Geophysics*, *64*(6), 1867–1876.

Kimmel, R., and Sethian, J. A. (1998). Computing geodesic paths on manifolds. *Proc. Natl. Acad. Sci. USA*, *95*(15), 8431–8435. https://doi.org/10.1073/pnas.95.15.8431

Knapp, C. C., Knapp, J. H., and Connor, J. A. (2004). Crustal-scale structure of the South Caspian Basin revealed by deep seismic reflection profiling. *Mar. Pet. Geol.*, *21*(8), 1073–1081. https://doi.org/10.1016/j.marpetgeo.2003.04.002

Koketsu, K., and Sekine, S. (1998). Pseudo-bending method for three-dimensional seismic ray tracing in a spherical earth with discontinuities. *Geophys. J. Int.*, *132*(2), 339–346. https://doi.org/10.1046/j.1365-246x.1998.00427.x

Lan, H. Q., and Zhang, Z. J. (2011a). Comparative study of the free-surface boundary condition in two-dimensional finite-difference elastic wave field simulation. *J. Geophys. Eng.*, *8*(2), 275–286. https://doi.org/10.1088/1742-2132/8/2/012

Lan, H. Q., and Zhang, Z. J. (2011b). Three-dimensional wave-field simulation in heterogeneous transversely isotropic medium with irregular free surface. *Bull. Seismol. Soc. Am.*, *101*(3), 1354–1370.

Lan, H. Q., Zhang, Z., Xu, T., and Bai, Z. M. (2012). Influences of anisotropic stretching of boundary conforming grid on traveltime computation by topography-dependent eikonal equation. *Chin. J. Geophys.*, *55*(5), 564–579. https://doi.org/10.1002/cjg2.1750

Lan, H. Q., and Zhang, Z. J. (2013a). Topography-dependent eikonal equation and its solver for calculating first-arrival traveltimes with an irregular surface. *Geophys. J. Int.*, *193*(2), 1010–1026. https://doi.org/10.1093/gji/ggt036

Lan, H. Q, and Zhang, Z. J. (2013b). A high-order fast-sweeping scheme for calculating first-arrival travel times with an irregular surface. *Bull. Seismol. Soc. Am.*, *103*(3), 2070–2082. https://doi.org/10.1785/0120120199

Lelièvre, P. G., Farquharson, C. G., and Hurich, C. A. (2011). Computing first-arrival seismic traveltimes on unstructured 3-D tetrahedral grids using the fast marching method. *Geophys. J. Int.*, *184*(2), 885–896. https://doi.org/10.1111/j.1365-246X.2010.04880.x

Li, S. L., and Mooney, W. D. (1998). Crustal structure of China from deep seismic sounding profiles. *Tectonophysics*, *288*(1-4), 105–113. https://doi.org/10.1016/S0040-1951(97)00287-4

Ma, T., and Zhang, Z. J. (2014a). Calculating ray paths for first-arrival travel times using a topography-dependent eikonal equation solver. *Bull. Seismol. Soc. Am.*, *104*(3), 1501–1517. https://doi.org/10.1785/0120130172

Ma, T., and Zhang, Z. J. (2014b). A model expansion criterion for treating surface topography in ray path calculations using the eikonal equation. *J. Geophys. Eng.*, *11*(2), 025007. https://doi.org/10.1088/1742-2132/11/2/025007

Ma, T., and Zhang, Z. J. (2015). Topography-dependent eikonal traveltime tomography for upper crustal structure beneath an irregular surface. *Pure Appl. Geophys.*, *172*(6), 1511–1529. https://doi.org/10.1007/s00024-014-0984-7

Podvin, P., and Lecomte, I. (1991). Finite difference computation of traveltimes in very contrasted velocity models: a massively parallel approach and its associated tools. *Geophys. J. Int.*, *105*(1), 271–284. https://doi.org/10.1111/j.1365-246X.1991.tb03461.x

Qian, J. L., and Symes, W. W. (2002). An adaptive finite-difference method for traveltimes and amplitudes. *Geophysics*, *67*(1), 167–176.

Qian, J. L., Zhang, Y. T., and Zhao, H. K. (2007a). A fast sweeping method for static convex Hamilton-Jacobi equations. *J. Sci. Comput.*, *31*(1-2), 237–271. https://doi.org/10.1007/s10915-006-9124-6

Qian, J. L., Zhang, Y. T., and Zhao, H. K. (2007b). Fast sweeping methods for Eikonal equations on triangular meshes. *SIAM J. Numer. Anal.*, *45*(1), 83–107. https://doi.org/10.1137/050627083

Qin, F. H., Luo, Y., Olsen, K. B., Cai, W. Y., and Schuster, G. T. (1992). Finite-difference solution of the eikonal equation along expanding wavefronts. *Geophysics*, *57*(3), 478–487.

Rawlinson, N., and Sambridge, M. (2004a). Multiple reflection and transmission phases in complex layered media using a multistage fast marching method. *Geophysics*, *69*(5), 1338–1350.

Rawlinson, N., and Sambridge, M. (2004b). Wave front evolution in strongly heterogeneous layered media using the fast marching method. *Geophys. J. Int.*, *156*(3), 631–647. https://doi.org/10.1111/j.1365-246X.2004.02153.x

Rawlinson, N., and Goleby, B. R. (2012). Seismic imaging of continents and their margins: New research at the confluence of active and passive seismology. *Tectonophysics*, *572-573*, 1–6. https://doi.org/10.1016/j.tecto.2012.07.021

Reshef, M. (1991). Depth migration from irregular surfaces with depth extrapolation methods. *Geophysics*, *56*(1), 119–122.

Riahi, M. A., and Juhlin, C. (1994). 3-D interpretation of reflected arrival times by finite-difference techniques. *Geophysics*, *59*(5), 844–849.

Sambridge, M. S. (1990). Non-linear arrival time inversion: Constraining velocity anomalies by seeking smooth models in 3-D. *Geophys. J. Int.*, *102*(3), 653–677. https://doi.org/10.1111/j.1365-246X.1990.tb04588.x

Scarascia, S., and Cassinis, R. (1997). Crustal structures in the central-eastern Alpine sector: a revision of the available DSS data. *Tectonophysics*, *271*(1-2), 157–188. https://doi.org/10.1016/S0040-1951(96)00206-5

Sethian, J. A. (1999). Fast marching methods. *SIAM Rev.*, *41*(2), 199–235. https://doi.org/10.1137/S0036144598347059

Sethian, J. A., and Vladimirsky, A. (2000). Fast methods for the Eikonal and related Hamilton–Jacobi equations on unstructured meshes. *Proc. Natl. Acad. Sci. USA*, *97*(11), 5699–5703. https://doi.org/10.1073/pnas.090060097

Symes, W. W., and Qian, J. L. (2003). A slowness matching eulerian method for multivalued solutions of eikonal equations. *J. Sci. Comput.*, *19*(1-3), 501–526. https://doi.org/10.1023/A:1025380731197

Teng, J. W., Wei, S. Y., Sun, K. Z., and Xue, C. S. (1987). The characteristics of the seismic activity in the Qinghai-Xizang (Tibet) Plateau of China. *Tectonophysics*, *134*(1-3), 129–144. https://doi.org/10.1016/0040-1951(87)90253-8

Teng, J. W., Zeng, R. S., Yan, Y. F., and Zhang, H. (2003). Depth distribution of Moho and tectonic framework in eastern Asian continent and its adjacent ocean areas. *Sci. China Ser. D Earth Sci.*, *46*(5), 428–446. https://doi.org/10.1360/03yd9038

Thompson, J. F., Warsi, Z. U. A., and Mastin, C. W. (1985). Numerical Grid Generation: Foundations and Applications. Amsterdam: North-Holland.

Tian, X. B., Teng, J. W., Zhang, H. S., Zhang, Z. J., Zhang, Y. Q., Yang, H., and Zhang K. K. (2011). Structure of crust and upper mantle beneath the Ordos Block and the Yinshan Mountains revealed by receiver function analysis. *Phys. Earth Planet. Inter.*, *184*(3-4), 186–193. https://doi.org/10.1016/j.pepi.2010.11.007

Um, J., and Thurber, C. (1987). A fast algorithm for two-point seismic ray tracing. *Bull. Seismol. Soc. Am.*, *77*(3), 972–986.

van Trier, J., and Symes, W. W. (1991). Upwind finite-difference calculation of traveltimes. *Geophysics*, *56*(6), 812–821.

Vidale, J. (1988). Finite-difference calculation of travel times. *Bull. Seismol. Soc. Am.*, *78*(6), 2062–2076.

Wang, C. Y., Zeng, R. S., Mooney, W. D., and Hacker, B. R. (2000). A crustal model of the ultrahigh-pressure Dabie Shan orogenic belt, China, derived from deep seismic refraction profiling. *J. Geophys. Res.*, *105*(B5), 10857–10869. https://doi.org/10.1029/1999JB900415

Wang, C. Y., Han, W. B., Wu, J. P., Lou, H., and Chan, W. W. (2007). Crustal structure beneath the eastern margin of the Tibetan Plateau and its tectonic implications. *J. Geophys. Res.*, *112*(B7), B07307. https://doi.org/10.1029/2005JB003873

Wu, C. L., Harris, J. M., Nihei, K. T., and Nakagawa, S. (2005). Two-dimensional finite-difference seismic modeling of an open fluid-filled fracture: Comparison of thin-layer and linear-slip models. *Geophysics*, *70*(4), T57–T62.

Xu, T., Xu, G. M., Gao, E. G., Li, Y. C., Jiang, X. Y., and Luo, K. Y. (2006). Block modeling and segmentally iterative ray tracing in complex 3D media. *Geophysics*, *71*(3), T41–T51. https://doi.org/10.1190/1.2192948

Xu, T., Zhang, Z. J., Gao, E. G., Xu, G. M., and Sun, L. (2010). Segmentally iterative ray tracing in complex 2D and 3D heterogeneous block models. *Bull. Seismol. Soc. Am.*, *100*(2), 841–850. https://doi.org/10.1785/0120090155

Xu, T., Li, F., Wu, Z. B., Wu, C. L., Gao, E. G., Zhou, B., Zhang, Z. J., and Xu, G. M. (2014). A successive three-point perturbation method for fast ray tracing in complex 2D and 3D geological models. *Tectonophysics*, *627*, 72–81. https://doi.org/10.1016/j.tecto.2014.02.012

Zelt, C. A., and Smith, R. B. (1992). Seismic traveltime inversion for 2-D crustal velocity structure. *Geophys. J. Int.*, *108*(1), 16–34. https://doi.org/10.1111/j.1365-246X.1992.tb00836.x

Zeng, R. S., Ding, Z. F., and Wu, Q. J. (1995). A review on the lithospheric structures in the Tibetan Plateau and constraints for dynamics. *Pure Appl. Geophys.*, *145*(3-4), 425–443. https://doi.org/10.1007/BF00879582

Zhang, W., and Chen, X. F. (2006). Traction image method for irregular free surface boundaries in finite difference seismic wave simulation. *Geophys. J. Int.*, *167*(1), 337–353. https://doi.org/10.1111/j.1365-246X.2006.03113.x

Zhang, Z. J., and Klemperer, S. L. (2005). West-east variation in crustal thickness in northern Lhasa block, central Tibet, from deep seismic sounding data. *J. Geophys. Res.*, *110*(B9), B09403. https://doi.org/10.1029/2004JB003139

Zhang, Z. J., and Klemperer, S. (2010). Crustal structure of the Tethyan Himalaya, southern Tibet: New constraints from old wide-angle seismic data. *Geophys. J. Int.*, *181*(3), 1247–1260. https://doi.org/10.1111/j.1365-246X.2010.04578.x

Zhang, Z. J., Deng, Y. F., Teng, J. W., Wang, C. Y., Gao, R., Chen, Y., and Fan, W. M. (2011). An overview of the crustal structure of the Tibetan plateau after 35 years of deep seismic soundings. *J. Earth Sci.*, *40*(4), 977–989. https://doi.org/10.1016/j.jseaes.2010.03.010

Zhou, B., Greenhalgh, S. A., and Sinadlnovskl, C. (1992). Iterative algorithm for the damped minimum norm, least-squares and constrained problem in seismic tomography. *Explor. Geophys.*, *23*(3), 497–505. https://doi.org/10.1071/EG992497